



OPEN

## Effects of normal stress on shear properties and acoustic emission characteristics of bonded rock-concrete interfaces

Yan Chen<sup>1,2,3✉</sup>, Jiangfan Yang<sup>1</sup>, Jintao Wang<sup>4</sup>, Shuai Heng<sup>1</sup> & Zhiqiang Hou<sup>1</sup>

Direct laboratory shear tests, accompanied by acoustic emission (AE) monitoring, were performed to examine the influence of normal stress (ranging from 4 to 16 MPa) on the shear behavior and acoustic emission characteristics of bonded granite-concrete interfaces. The findings indicate that an increase in normal stress correlates linearly with enhancements in peak shear strength, residual strength and shear stiffness, while also facilitating a transition from ductile to brittle modes. Furthermore, elevated normal stress induced a 'double peak stress' phenomenon following softening, which intensified the degree of interfacial damage. AE analyses indicate that peak shear stress is responsible for generating high-energy AE signals, while the cumulative AE energy exhibits a slight increase prior to failure. Conversely, the cumulative AE count diminishes under elevated normal stresses. The b value and F-function serves as an effective indicator of crack evolution; The significant decrease in b-value at peak stress and the significant increase in F-value at peak stress are associated with brittle damage. Additionally, the proportion of shear damage signals in specimens, as determined by the joint Gaussian Mixture Model (GMM) and Support Vector Machine (SVM), was found to exceed 75% and to rise with higher normal stress levels. These findings underscore the significant influence of normal stress on the brittle-ductile transition and the degree of interfacial damage, thereby providing theoretical insights for the optimization of tunnel lining design in the context of high geostatic stresses.

**Keywords** Bonded rock-concrete interface, Shear failure mechanism, Normal stress, Acoustic emission characteristics

The interface between concrete and the adjacent rock constitutes a vulnerable joint within the tunnel support system, primarily due to the reduction in thickness of the sprayed layer. This interface is particularly prone to shear failure when subjected to the pressures exerted by the surrounding rock and the excavation gap<sup>1–6</sup>. The shear stress present at this interface can precipitate various engineering geological failures, including lining fractures, bottom bulging, and cave-ins, which ultimately compromise the overall structural integrity and stiffness. Conversely, the application of a specific range of normal stresses can enhance the density of the rock mass and subsequently increase its shear strength<sup>7–11</sup>. Consequently, examining the shear characteristics and fracture behavior of bonded rock-concrete interfaces holds significant practical importance.

The primary determinants influencing interfacial shear strength can be categorized into two distinct groups: internal factors, which encompass the characteristics of rock surface roughness and material properties, and external factors, which pertain to the state of interface forces, such as normal stress and loading rate<sup>12–14</sup>. An increase in normal stress enhances shear strength by augmenting interfacial sliding friction resistance and the mechanical interlocking effect associated with rough interfaces. However, as normal stress reaches a certain threshold, the nature of interface damage shifts from relative slip to extensive nibbling damage. Consequently, there exists a paucity of research addressing the shear damage behavior and crack propagation behavior of rock-concrete interfaces under elevated normal stresses for bonded surfaces exhibiting specific roughness<sup>9–10</sup>. In recent years, numerous scholars have conducted a series of shear tests on rock-concrete interfaces subjected

<sup>1</sup>School of Energy Science and Engineering, Henan Polytechnic University, Jiaozuo 454000, People's Republic of China. <sup>2</sup>Henan Key Laboratory for Green and Efficient Mining & Comprehensive Utilization of Mineral Resources, Henan Polytechnic University, Jiaozuo 454000, People's Republic of China. <sup>3</sup>Collaborative Innovation Center of Coal Work Safety and Clean High Efficiency Utilization, Henan Polytechnic University, Jiaozuo 454000, People's Republic of China. <sup>4</sup>School of Civil Engineering, Ludong University, Yantai 264025, People's Republic of China. <sup>✉</sup>email: chenyan@hpu.edu.cn

to varying normal stresses, yielding significant findings related to interfacial shear mechanisms, damage characteristics, and fracture mechanical properties<sup>15–19</sup>. For instance, Saiang et al.<sup>20</sup> examined the shear damage behavior of rock-concrete interfaces through shear, tensile, and compression tests under bonded conditions. Their findings indicated that, at lower normal stresses, shear strength is predominantly governed by the bond strength between rock and concrete, whereas at higher normal stresses, shear strength is influenced by a combination of bond strength and friction. Tian et al.<sup>21</sup>, Bost et al.<sup>22</sup>, and Mouzannar et al.<sup>23</sup> examined the bond strength between rock and concrete utilizing a smooth granite interface, revealing that the shear strength of this interface is significantly correlated with bond strength when the normal stress is below 6 MPa. Johansson et al.<sup>24</sup> identified that the residual behavior observed was attributable to the purely frictional interactions at the unbonded concrete-rock contact under low normal loads. Sun et al.<sup>25</sup> analyzed the linear response of stress-expansion at the soil-structure interface under varying loading conditions, noting that considerable softening of the interface occurred irrespective of the initial normal stress. Alonso et al.<sup>26</sup> performed direct shear tests on clay-concrete contact surfaces, discovering that the maximum shear stress at the interface increased with rising normal stress. Liu et al.<sup>27</sup> executed cyclic normal stress shear damage tests on coarse-walled sandstone cracks. Wu et al.<sup>28</sup> conducted direct shear tests on a simulated granular channel to investigate the mechanisms that initiate dynamic slip, finding that the sliding behavior is significantly affected by normal stress once the shear stress surpasses a critical threshold. Collectively, these studies offer essential data and insights into the shear damage characteristics of rock-concrete interfaces under low normal stress conditions. However, there is a paucity of shear tests aimed at assessing the impact of high normal stress conditions on the shear strength and crack propagation behavior of concrete-rock interfaces in a bonded state.

Despite notable advancements in the characterization of the macroscopic mechanical properties of the bonded rock-concrete interface, primarily through laboratory testing methods and conditions, there remains a significant gap in the understanding of the micromechanical behavior of this interface and its regulatory mechanisms influencing macroscopic strength and deformation responses. Recent developments in multi-scale joint testing technology have introduced a novel framework for elucidating the damage evolution mechanisms at the bonded rock-concrete interface. Techniques such as high-speed video imaging, X-ray computed tomography (CT), acoustic emission (AE), and digital image correlation (DIC) have been employed to explore the correlation between macroscopic behaviors and microscopic fracture characteristics. Acoustic emission signals, which are transient elastic waves produced by the rapid release of energy during material fracture, play a crucial role in the continuous monitoring of elastic waves generated by microcracks, thereby aiding in the prediction of cracking in tunnel linings<sup>29–31</sup>. However, the application of this technique to monitor shear mechanisms at bonded rock-concrete interfaces has been limited. For instance, Changwoo et al.<sup>32</sup> investigated the acoustic emission characteristics of rock-concrete interfaces subjected to shear loading, revealing that the AE count rate and energy peaked when the stress decreased following the maximum shear stress. Similarly, Moradian et al.<sup>9,10</sup> examined the damage mechanisms of rock joints and concrete-rock bond joints during shear tests utilizing AE equipment. Gan et al.<sup>33</sup> analyzed the temporal patterns of RA and AF values, discussing criteria for differentiating between shear and tensile cracks. Furthermore, Cheng et al.<sup>34</sup> identified that the warning point of AE energy and a significant decline in AE-b values typically occurred in proximity to the continuous stress drop or peak stress.

In summary, a standard granite specimen was utilized as a bonded granite-concrete sample and subjected to direct shear testing under normal stress conditions of 4 MPa, 8 MPa, 12 MPa, and 16 MPa. The entire shear damage process was monitored using acoustic emission technology to enhance the understanding of the shear failure mechanisms at the rock-concrete bonded interface. This study primarily investigates the shear mechanical properties and fracture behavior of the rock-concrete interface under varying normal stress levels. The experimental findings offer significant theoretical insights into the shear behavior of the rock-concrete interface and provide essential guidance for the design and maintenance of engineering structures.

## Experimental testing

### Preparation process of rock-concrete specimens

The rock-concrete specimens utilized in the experimental investigations are composed of gray granite and self-compacting concrete materials. The gray granite is sourced from a stone processing facility located in Wulian County, Shandong Province, China. This granite exhibits a fine-grained texture, with a particle size distribution ranging from 0.5 to 1 mm. X-ray diffractometry (XRD) analysis indicates that the gray granite is comprised of quartz, albite, dolomite, kaolinite, and various other minerals. For the experiments, cylindrical granite specimens with a diameter and height of 50 mm are prepared through drilling, cutting, and polishing techniques. Furthermore, the concrete employed in the tests is a high-strength self-compacting concrete, specifically formulated for applications that present challenges in pouring, such as underground excavations characterized by dense reinforcement and intricate geometries. The concrete mixture consists of 45.36% cement, 35.81% aggregate, 8.12% sand, and 10.71% water, with the maximum particle size of the coarse aggregate being 5 mm. Figure 1 depicts the rock-concrete specimens utilized in the experiment, while Table 1 provides the mechanical and uniaxial compressive properties of both gray granite and concrete. Figure 2 illustrates that the stress-strain curves of the rock-concrete specimens under uniaxial loading exhibit brittle failure characteristics akin to those of monolithic rock. However, as confining pressure increases, the rock-concrete specimens progressively transition to ductile failure. Additionally, the relationship curve between rock and concrete approaches that of concrete, suggesting that the deformation and failure mode of the rock-concrete composite is predominantly influenced by the lower strength concrete. It is important to note that the fracture morphology of the rock, concrete, and rock-concrete composite specimens under both uniaxial and triaxial compression is comprehensively detailed in reference<sup>35</sup>.

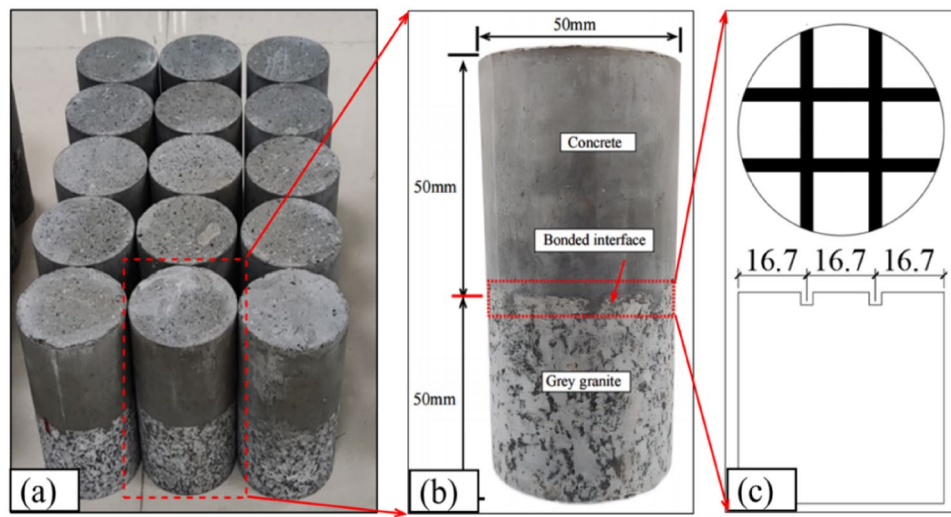


**Fig. 1.** The experimental study utilized rock-concrete specimens, which included: (a) the rock-concrete specimens employed in the shear test, (b) a standard cylindrical sample of rock-concrete, and (c) the grooving treatment applied to the rock interface.

materials	$\sigma_c$ (MPa)	E(GPa)	$\mu$	$\rho$ (kg/m <sup>3</sup> )
gray granite	185	57	0.286	0.687
concrete	98	30	0.158	0.580
gray granite- concrete	100	29	0.164	0.634

**Table 1.** The uniaxial compression characteristics of Gray granite and concrete are defined by several key parameters:  $\sigma_c$  represents the uniaxial compressive strength, E denotes the elastic modulus of the material,  $\mu$  indicates the poisson's ratio, and  $\rho$  signifies the density of the material.

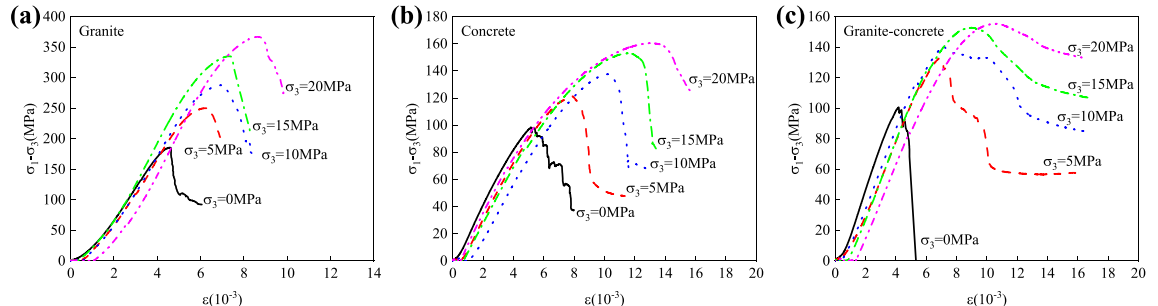


**Fig. 2.** The stress-strain relationships for rock, concrete, and rock-concrete composite materials subjected to uniaxial and triaxial compression are presented as follows: (a) specimens of rock, (b) specimens of concrete, and (c) specimens of rock-concrete composites<sup>35</sup>.

### Experimental facilities

The shear test is performed utilizing the GCTS RDS-200 servo-controlled loading system (refer to Fig. 3(b)). This testing apparatus is equipped with a shear actuator and a normal actuator, capable of delivering loads of 10 tons and 5 tons, respectively, with a precision of 0.01 kN. The system allows for a maximum shear displacement of 25 mm and a normal displacement of 24 mm, both with a measurement accuracy of 0.001 mm.

Acoustic emissions are monitored utilizing an 8-channel PAC system. The configuration of the AE sensor, preamplifier, signal cable, and AE hardware system is illustrated in Fig. 3(b). As depicted in Fig. 3(a), the eight AE sensors are securely affixed to the designated monitoring points on the upper shear box using medical couplers. To mitigate the influence of environmental noise and various interference signals, the detection threshold of the system is established at 35 dB, with a sampling rate of 1 million samples per second. The sensitivity of each sensor is evaluated through a lead break test, with the requirement that the response amplitude of each channel exceeds

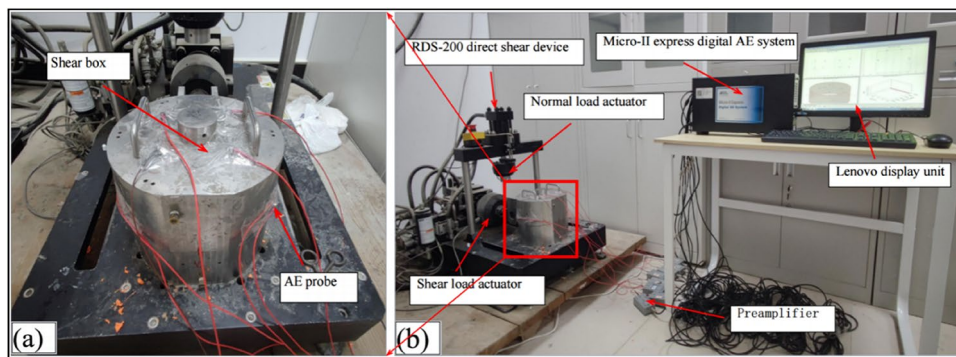


**Fig. 3.** Instrument used for test **(a)** eight AE sensors are arranged in the upper shear box, **(b)** GCTS RDS-200 test system and acoustic emission test system.

95 dB. Additionally, it should be noted that the acoustic emission sensor model used in this paper is MINI30 and that the acoustic emission signals are acquired and parameterized by hit.

### Experimental process

In this investigation, the rock-concrete specimens are categorized into four distinct groups based on variations in normal stress, with three parallel tests conducted for each level of normal stress to enhance the accuracy and reliability of the findings. The detailed experimental procedure is outlined as follows:

- (1) As depicted in Fig. 3(a), prior to the initiation of the shear test, it is imperative to position the sample centrally within the shear box. Consequently, the encapsulated sample is initially placed in the shear box to ensure that the bond surface between the rock and concrete is situated within the cavity of both the upper and lower shear boxes, aligned parallel to the direction of shear.
- (2) Following this, a normal compressive stress of 4 MPa, 8 MPa, 12 MPa, and 16 MPa is applied in a load control mode, with a loading rate of 1 MPa/min for each respective stress level.
- (3) Subsequently, the shear load is applied using displacement control at a shear rate of 1 mm/min, with the test concluding once the shear displacement reaches 10 mm.
- (4) At the commencement of stage (3), the acoustic emission (AE) testing system is activated to capture AE signals, including AE count and AE energy.

### Shear failure properties of granite-concrete interface

#### Shear stress-shear displacement curves

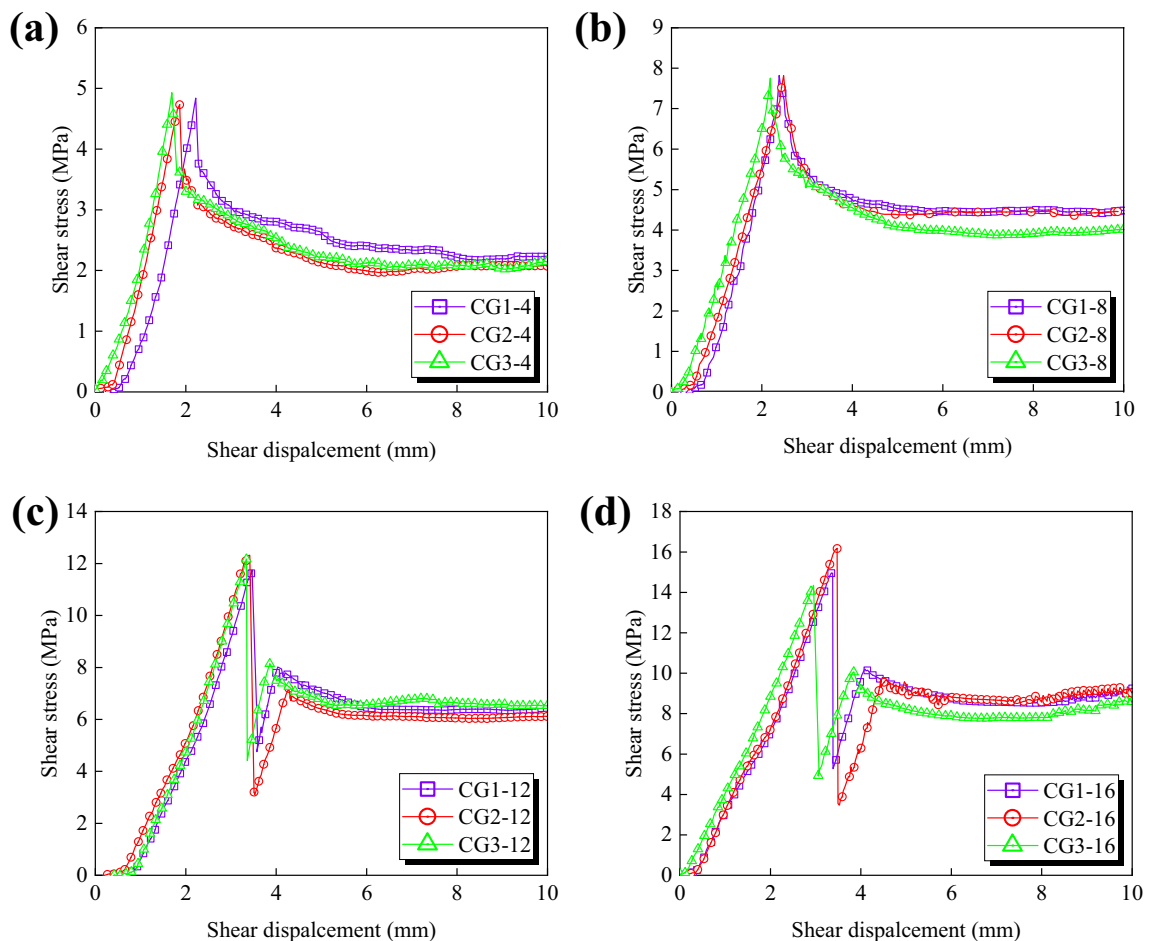
Figure 4 illustrates the shear stress versus horizontal displacement curves corresponding to four distinct normal stresses, which can be categorized into four distinct stages: the compaction stage, the linear elastic stage, the pre-peak plasticity stage, and the post-peak softening stage. During the compaction stage (OA), the stress-displacement curve exhibits a concave shape, signifying the gradual compression of cracks within the specimen. As the normal stress increases, the duration of compaction during this stage diminishes. In the linear elastic stage (AB), there is a linear increase in shear stress with respect to displacement. The pre-peak plasticity stage (BC) is characterized by an accelerating growth rate of shear stress, culminating in the attainment of peak shear strength. In the post-peak softening stage (CF), the behavior of the curve varies with normal stress levels. At lower normal stresses (4 MPa and 8 MPa), the curve demonstrates a post-peak plunge behavior, as depicted in Fig. 5(a), where the shear stress gradually declines to the residual strength following the peak. Conversely, at higher normal stresses (12 MPa and 16 MPa), the curve exhibits a post-peak rebound behavior, illustrated in Fig. 5(b), where the shear stress experiences a sharp decline until the displacement is regulated again at the predetermined shear rate, subsequently rising to a new peak stress, thereby exhibiting a “primary and secondary double peak” phenomenon.

### Shear parameters of the interface

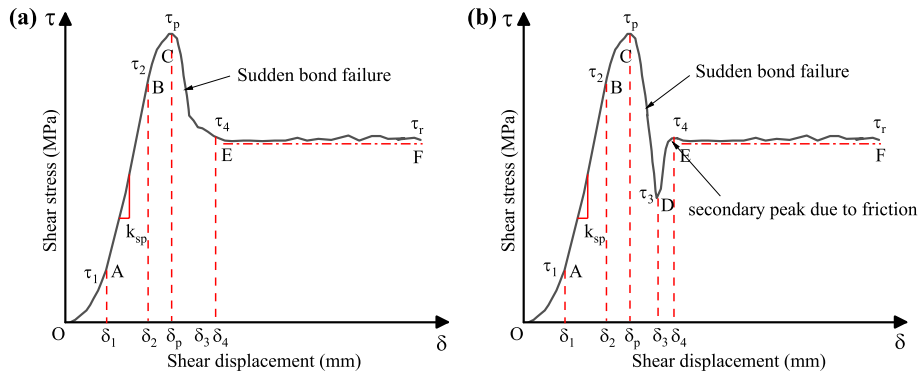
The mean values of test outcomes, including peak stress ( $\tau_p$ ), residual stress ( $\tau_r$ ), and shear stiffness ( $k_{sp}$ ), for the twelve specimens are presented in Table 2. To conduct a more in-depth examination of the effect of normal stress on the shear properties of the specimen interface, the correlation between the different shear test parameters and surface roughness is illustrated in Fig. 6.

Figure 6(a) illustrates a linear relationship between peak shear stress and normal stress, indicating that the latter enhances mechanical interlocking at both sides of the interface. As normal stress increases, a greater number of bulges are compromised through shearing during the dislocation of the rock-concrete interface, thereby augmenting the interface's resistance to shear failure. Furthermore, in accordance with the Mohr-Coulomb criterion, the internal friction angle of the assembly is determined to be 40.86°, with a cohesion value of 0.87 MPa.

In this study, the slope of the curve at 50% of the peak shear strength is utilized to define the pre-peak shear stiffness, which serves as an indicator of the sample's resistance to deformation during the shearing process.



**Fig. 4.** The shear stress-displacement relationships were analyzed under four distinct normal stress conditions: (a) 4 MPa, (b) 8 MPa, (c) 12 MPa, and (d) 16 MPa.

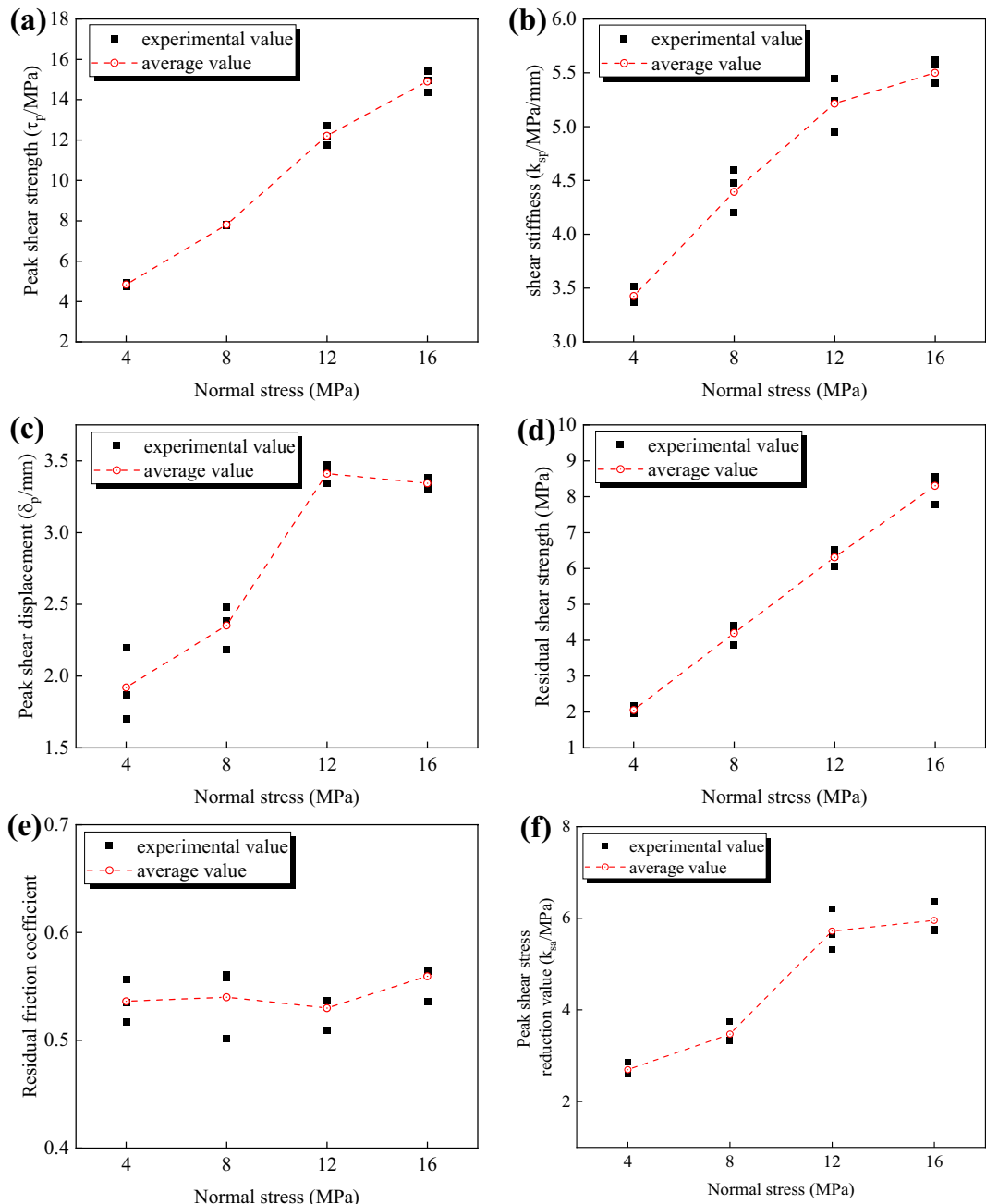


**Fig. 5.** Two kinds of shear stress-displacement curves of rock-concrete under bonded state (a) sudden decline type after the peak, (b) rebound type after the peak.

Figures 6(b) and 6(c) demonstrate that both pre-peak shear stiffness and peak shear displacement exhibit an increase with rising normal stress, followed by a gradual stabilization.

The residual strength is primarily attributed to the frictional interactions at the contact surface, rendering it dependent solely on normal stress. As depicted in Fig. 6(d), the residual strength shows a strong linear correlation with normal stress. The average residual shear strengths recorded under varying normal compressive stresses were 2.144 MPa, 4.320 MPa, 6.358 MPa, and 8.950 MPa, corresponding to increase rates of 101.490%, 47.180%, and 40.771%, respectively. Additionally, Fig. 6(e) indicates that the interface friction coefficient during the residual stage remains relatively constant at 0.526, suggesting that the roughness of the interface does not

Sample	$\tau_p$ (MPa)	$\tau_r$ (MPa)	$\delta_p$ (mm)	$k_{sp}$ (MPa/mm)	$k_{sa}$ (MPa)
CG-4	4.84	2.05	1.92	3.43	3.69
CG-8	7.79	4.20	2.35	4.43	3.47
CG-12	12.08	6.31	3.41	5.21	5.72
CG-16	14.90	8.26	3.35	5.54	5.95

**Table 2.** The average value of the test results of each specimen.**Fig. 6.** The variation of computed shear parameters includes: (a) peak shear strength, (b) shear stiffness, (c) peak shear displacement, (d) residual shear strength, (e) residual friction coefficient, and (f) the reduction value of peak shear stress.

significantly change, and that the friction coefficient at the contact surface is independent of normal compressive stress.

When the shear stress attains the bonded strength of the interface, a sudden failure of the entire interface bond occurs, resulting in a rapid decline in shear stress. To quantitatively assess this phenomenon, the post-peak stress drop ( $k_{sa}$ ), as illustrated in Fig. 6(f), is employed to denote the disparity between peak strength and residual strength. The average post-peak stress drops observed under varying normal stresses are 2.691 MPa, 3.347 MPa, 5.720 MPa, and 5.953 MPa, with corresponding increases of 2.040%, 113.062%, and 6.156%, respectively. These findings suggest that as normal stress increases, the extent of reduction in peak shear stress upon assembly failure also escalates. This trend can be attributed to the transition of the failure mode of the assembly from ductile to brittle as normal stress intensifies. Furthermore, it is noteworthy that the post-peak stress reduction observed in specimens subjected to 12 MPa is significantly greater than that in those subjected to 8 MPa. This observation indicates that once normal stress reaches a certain threshold, the accumulated elastic deformation energy within the rock-concrete composite is released rapidly and violently during the stress drop phase, thereby exhibiting characteristics of brittle failure (Table 3).

### Normal deformation characteristics of interface

Figure 7 illustrates the typical displacement-shear displacement curves of bonded surfaces subjected to varying normal stress levels. This observation is consistent with the shear testing performed by Liu et al.<sup>36</sup> on the interface between reef limestone and concrete under normal stress conditions. In the present study, the normal displacement at the initiation of shearing is regarded as the reference point for the curve. A positive slope of the curve signifies normal shear-shrinkage deformation, whereas a negative slope denotes normal shear-dilation deformation. The specific principles governing these behaviors are outlined as follows:

The application of normal stress to the specimen precedes the initiation of shear. Consequently, during the initial shear phase, the bonding interface experiences volumetric compression deformation, which intensifies with increasing normal stress. Furthermore, as illustrated in Fig. 8(a), the relationship depicted by the curve demonstrates a strong linear correlation. The normal displacements recorded prior to shear under varying normal stress conditions are 1.261 mm, 2.184 mm, 3.015 mm, and 4.217 mm, respectively.

In scenarios characterized by low normal stress (4 MPa and 8 MPa), the curve indicates a progression from initial shear deformation to subsequent dilatancy deformation. This phenomenon can be attributed to the relatively low normal binding forces acting on either side of the specimen, which facilitates the occurrence of a slope-climbing effect at the rock-concrete bonding interface following the establishment of a macro-shear fracture surface.

Conversely, under conditions of elevated normal stress (12 MPa and 16 MPa), there is a pronounced variability in normal deformation. This includes shear deformation (CG1-12, CG2-12), dilatation deformation (CG2-16, CG3-16), and initial shear deformation following dilatation (CG3-12, CG1-16). Such variability may be linked to the intricate and unpredictable nature of local peel wear at the interface. When normal stress levels are excessively high (CG2-16, CG3-16), it is possible for the interface to sustain partial fracture prior to the

Normal stress ( MPa )	1		2		3		Direction of shear
4							
8							
12							
16							

**Table 3.** The analysis of the distribution area of adherent concrete was conducted utilizing Image-Pro Plus image processing software.

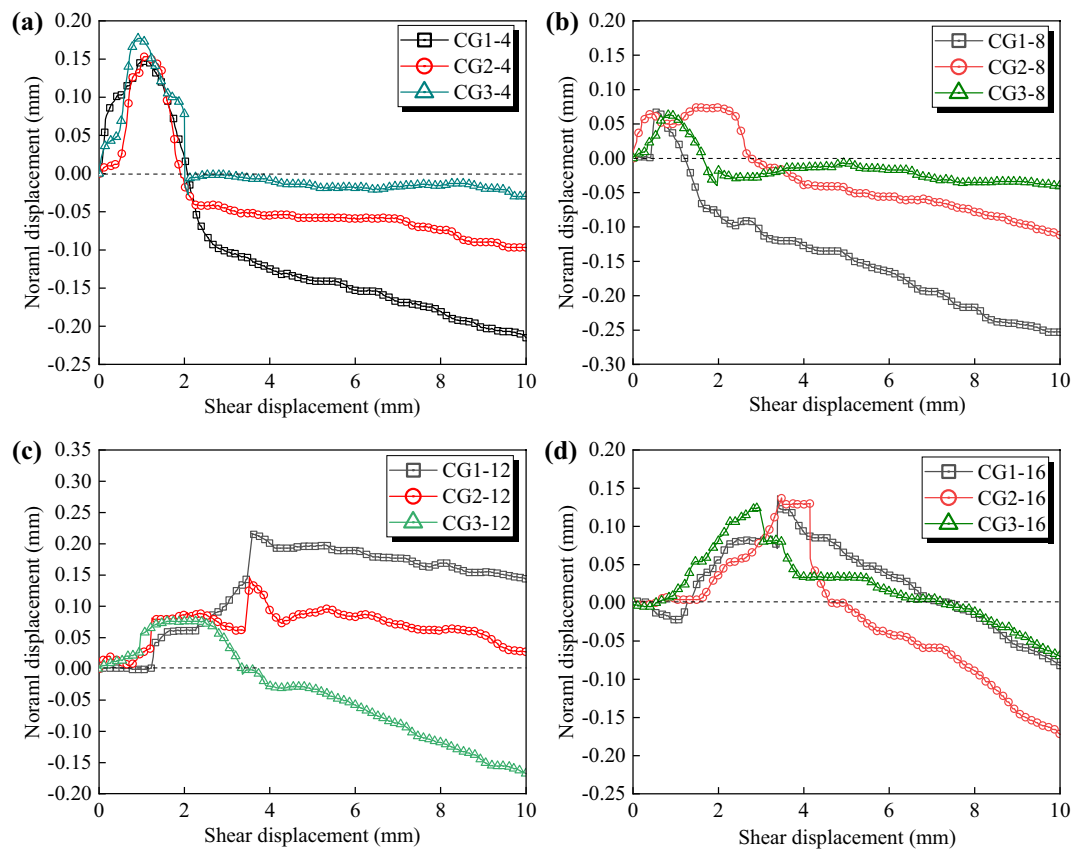


**Fig. 7.** Normal displacement-shear displacement of bonded surfaces **(a)** 4 MPa, **(b)** 8 MPa, **(c)** 12 MPa, **(d)** 16 MPa.

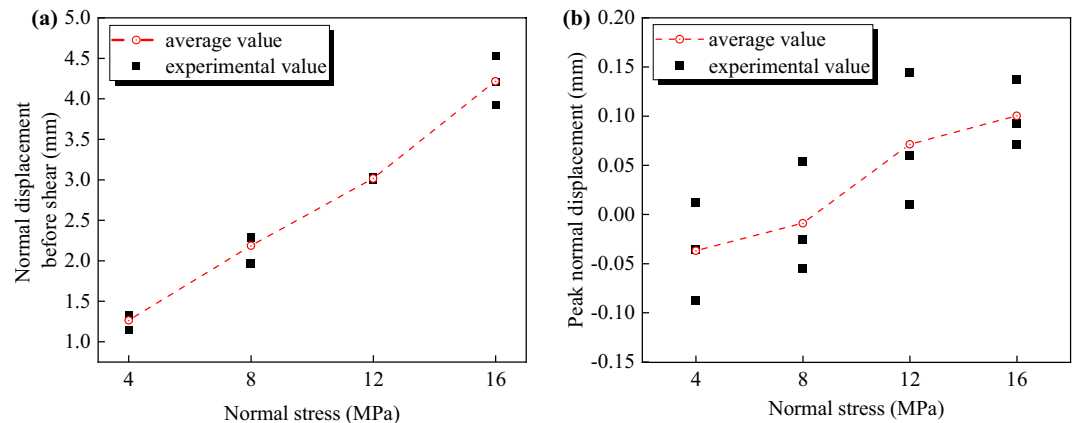


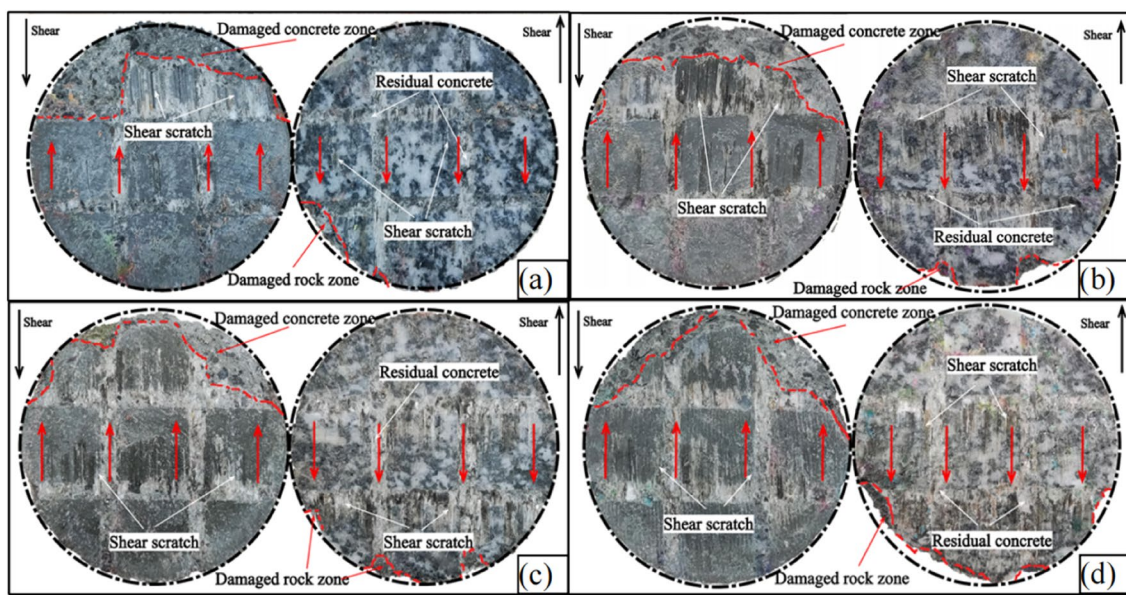
**Fig. 8.** The normal displacement was computed as a function of normal displacement, specifically addressing **(a)** the normal displacement prior to shear and **(b)** the maximum normal displacement observed.

application of shear stress, leading to uncrushed concrete protrusions that are susceptible to spanning and climbing during the shear process.

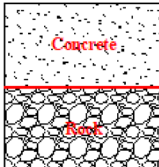
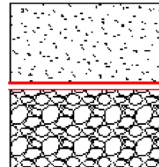
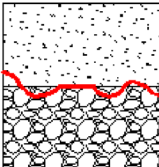
As depicted in Fig. 8(b), the specimen demonstrates dilatancy under conditions of low normal stress, while exhibiting pronounced shear shrinkage behavior under conditions of high normal stress.

#### Shear failure characteristics of the interface

The damaged regions of the concrete and rock are illustrated by the red dotted lines and black boundaries in Fig. 9. The left side of each interface represents the concrete component, while the right side corresponds to the rock component. Figure 9 clearly indicates that all specimens have sustained fractures along the rock-concrete



**Fig. 9.** The attributes of the shear failure interface between rock and concrete are illustrated, with the left side of each figure depicting the damaged concrete interface and the right side representing the damaged rock interface. The figures are labeled as follows: (a) CG1-4, (b) CG3-8, (c) CG3-12, and (d) CG1-16.

Failure Mode	Failure Evaluation
Adhesive failure	 <p>Failure at adhesion interfaces between rock and concrete when adhesion is low</p>
Cohesive failure in concrete and adhesive failure	 <p>Failure at concrete and adhesion interfaces when adhesion interfaces is higher than the concrete itself</p>
Mixed failure	 <p>Failure at concrete, rock and adhesion interfaces between rock and concrete when adhesion is high</p>

**Table 4.** Categorization of failure mechanisms associated with bonding interfaces<sup>35</sup>.

bonded interface. Furthermore, both the rock and concrete surfaces exhibit varying levels of damage. Notably, the protruding features of the rocks have compromised the low-strength concrete bulges, resulting in distinct gray scratches on the uncut surfaces.

The interfacial shear fracture morphology of the specimens subjected to four different normal stresses displayed a consistent ARC-type mixed damage pattern, as detailed in Table 4<sup>35</sup>. This observation suggests that the macroscopic failure mode of the interface is not influenced by the level of normal stress. It is particularly

noteworthy that, in comparison to the normal stress of 4 MPa, the damage area at the rock interface edge significantly increases at 16 MPa. This phenomenon can be attributed to the fact that the rock-concrete interface, being a weak surface, experiences substantial local compressive deformation during the normal loading phase as normal stress increases, thereby rendering the interface more susceptible to damage under shear loading. Additionally, the edge fractures at the interface, resulting from stress concentration, become increasingly pronounced with the rise in normal stress.

The red region depicted in Table 3 illustrates the distribution area of adherent concrete, which was examined utilizing Image-Pro Plus image processing software. The residual ratio of concrete present on the rock surface is defined as the proportion of the concrete surface area relative to the granite surface area on the rock. The corresponding formula is presented as follows:

$$\beta = \frac{S_c}{S_r} \quad (1)$$

where  $S_r$  denotes the projected area of the undamaged rock grooving surface, and  $S_c$  represents the projected area of concrete adhering to the rock surface.

Figure 9; Table 3 illustrate that an increase in normal stress correlates with a more pronounced damage to the rock and concrete, as well as an increase in surface scratches. Furthermore, as depicted in Fig. 10, there is a slight upward trend in the concrete residual rate at the rock interface with increasing normal stress; however, the overall average value remains approximately 30%. This indicates that the degree of damage to the rock-concrete interface escalates with varying levels of normal stress.

### Acoustic emission characteristics of the interface

#### Variation of AE energy and AE count during the shearing process

Figures 11 and 12 illustrate that the acoustic emission (AE) curve types under varying normal stresses consistently exhibit a burst pattern, suggesting that alterations in normal stress do not significantly affect the types of AE curves observed. Building on the findings of Zhou et al.<sup>37</sup>, the cumulative AE signal curve can be categorized into four distinct phases: the quiet period, the slow rise period, the sharp growth period, and the rapid rise period.

- (1) Compaction Stage: During the initial shear phase, AE signals from specimens subjected to normal stresses of 8 MPa, 12 MPa, and 16 MPa were scarcely detectable. At lower normal stresses, the inherent micropores within the specimen remain relatively sparse under normal loading conditions, resulting in minimal AE signals under minor shear forces. As normal stress increases, the density of the rock-concrete interface gradually improves, rendering minor shear forces insufficient to induce displacement at the interface. Consequently, there is a reduced occurrence of AE events during this stage, indicating limited crack activity within the specimen.
- (2) Linear Elastic Stage: The cumulative AE energy and AE count curves for each level of normal stress exhibit a relatively stable growth trend; however, prominent AE signals remain absent.
- (3) Pre-Peak Plasticity Stage: Specimens subjected to varying normal stresses do not display a distinct yield stage, suggesting that the elastic deformation energy of the materials in this phase is not fully dissipated.
- (4) Post-Peak Softening Stage: Following the failure of the rock-concrete bond interface, both AE energy and AE count decline to a lower level. Nevertheless, AE activity is observed to be higher than prior to interface failure, indicating a rapid increase in the accumulated AE energy curve. The AE signals during this phase primarily arise from the sliding friction at the contact surface, with few new cracks being generated, resulting in limited prominent AE energy production following the peak stress.

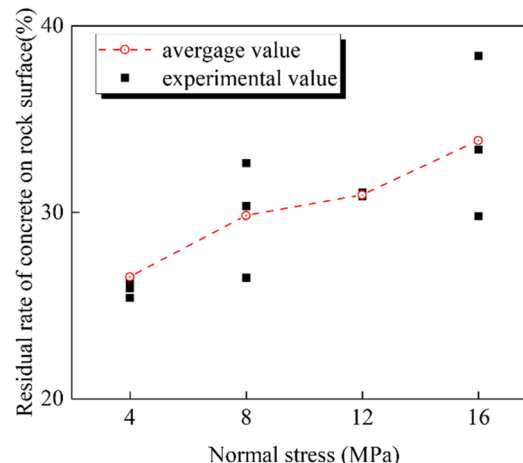


**Fig. 10.** The concrete residual rate at the rock interface.

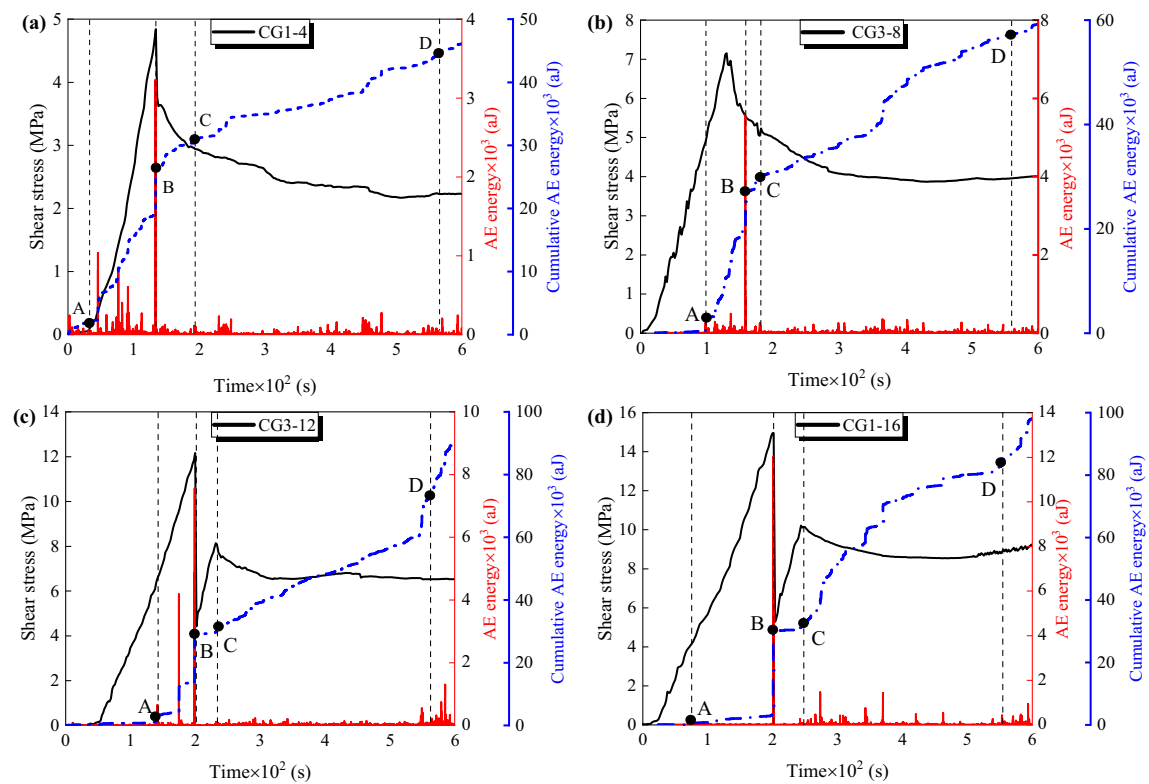


**Fig. 11.** The acoustic emission (AE) energy was computed as a function of displacement for four distinct levels of normal stress, specifically: (a) CG1-4, (b) CG3-8, (c) CG3-12, and (d) CG1-16.

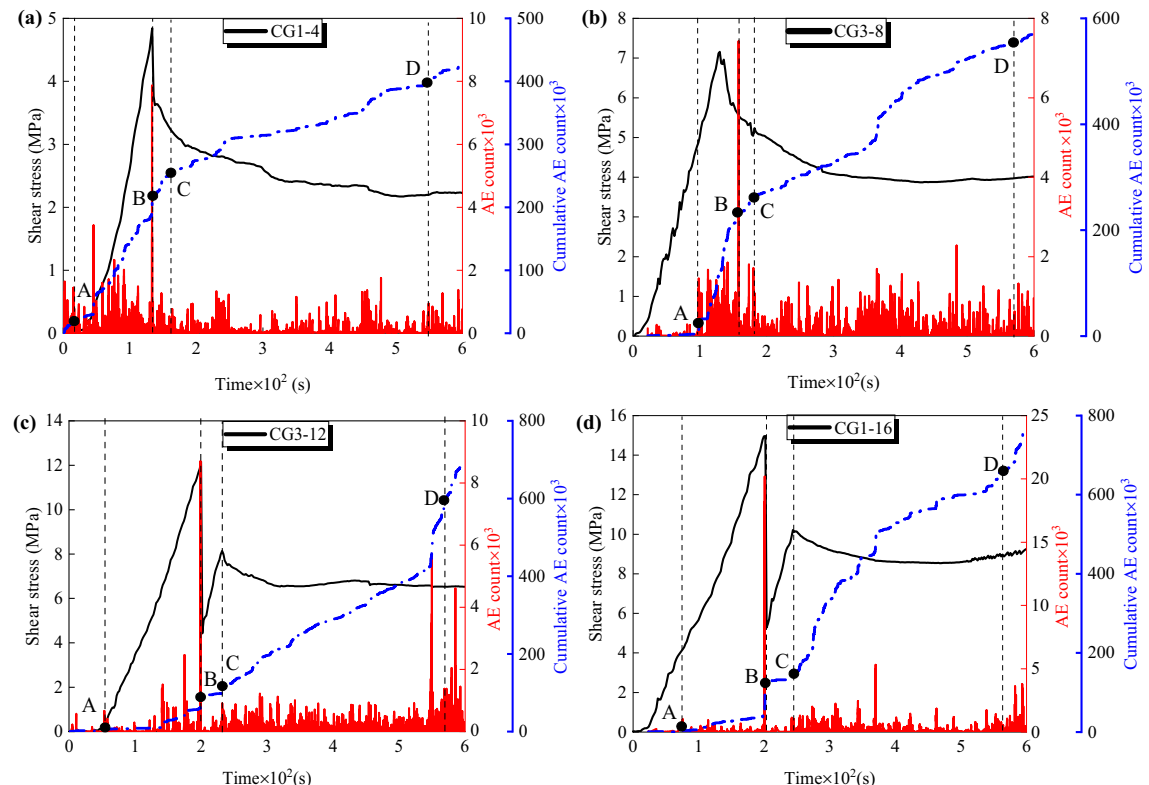


**Fig. 12.** The acoustic emission (AE) count was computed as a function of displacement for four distinct normal stress conditions: (a) CG1-4, (b) CG3-8, (c) CG3-12, and (d) CG1-16.

Figures 13(a) and (b) illustrate a comparable pattern in the variations of acoustic emission (AE) energy and count curves, both exhibiting a pronounced increase at the peak shear stress. Furthermore, Figs. 13(c) and 13(d) indicate that both the peak energy counts and peak counts of AE rise in conjunction with increasing normal stress.

Analysis of Fig. 14(a) and (b) reveals that the growth rate of the cumulative AE energy and cumulative AE count curves diminishes as normal stress increases prior to reaching the peak stress. This observation suggests that elevated normal stress serves to inhibit the propagation of cracks within the material to a certain degree, thereby enhancing the material's resistance to shear failure and reducing its susceptibility to fracture damage, which in turn delays the release of internal energy. Upon reaching the peak shear strength, the cumulative acoustic emission energy exhibits a gradual increase with rising normal stress. Following the damage to the rock-mix interface, the trajectory of the cumulative acoustic emission energy curve diverges from that observed prior to fracture; specifically, higher normal stress correlates with more extensive crack propagation and increased damage. The cumulative acoustic emission behavior prior to peak shear stress is depicted in Fig. 14(c), which demonstrates a significant increase in cumulative AE energy with rising normal stress. Conversely, Fig. 14(d) illustrates a declining trend in cumulative AE ring counts prior to the peak as normal stress increases.

### Variation of the AE b-value and F-function in the shear process

The AE b-value is acknowledged as a significant parameter in the examination of crack development in both rock and concrete materials. This metric was initially formulated for seismological purposes, drawing upon the principles established in the Gutenberg-Richter relationship<sup>38</sup>:

$$\lg N = a - bM \quad (2)$$

In this context, let  $M$  represent the magnitude of an earthquake,  $N$  denote the number of earthquakes within a specified magnitude range  $M + \Delta M$ ,  $a$  signify the constant associated with the degree of seismic activity, and  $b$  refer to the b-value utilized in seismological studies. When determining the b-value for acoustic emissions (AE), it is customary to divide the amplitude of the AE by 20 in order to substitute for the  $M$ -value<sup>39</sup>–<sup>40</sup>. Consequently, in accordance with Eq. (2), the formula for calculating the b-value of AE can be articulated as follows:

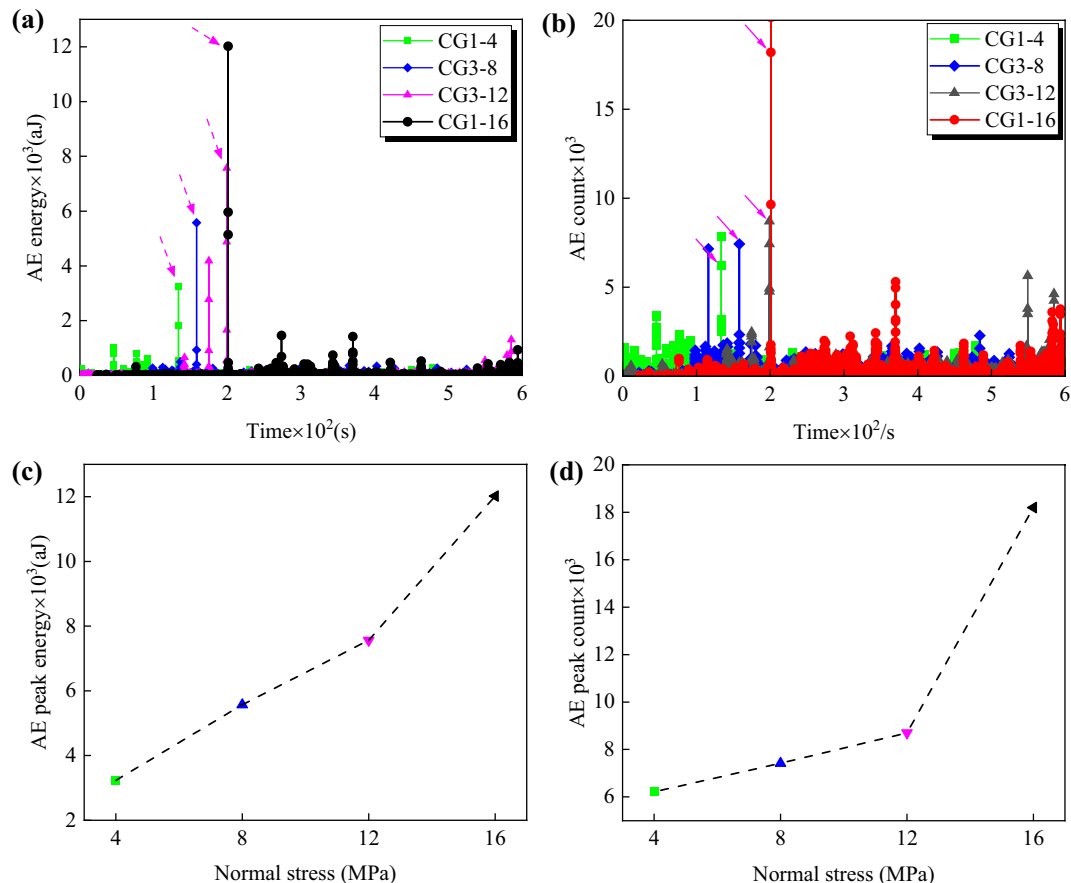


**Fig. 13.** The analysis of AE data encompasses the following components: (a) a comparative assessment of AE energy curves, (b) a comparative evaluation of AE count curves, (c) the determination of peak AE energy, and (d) the quantification of peak AE counts.

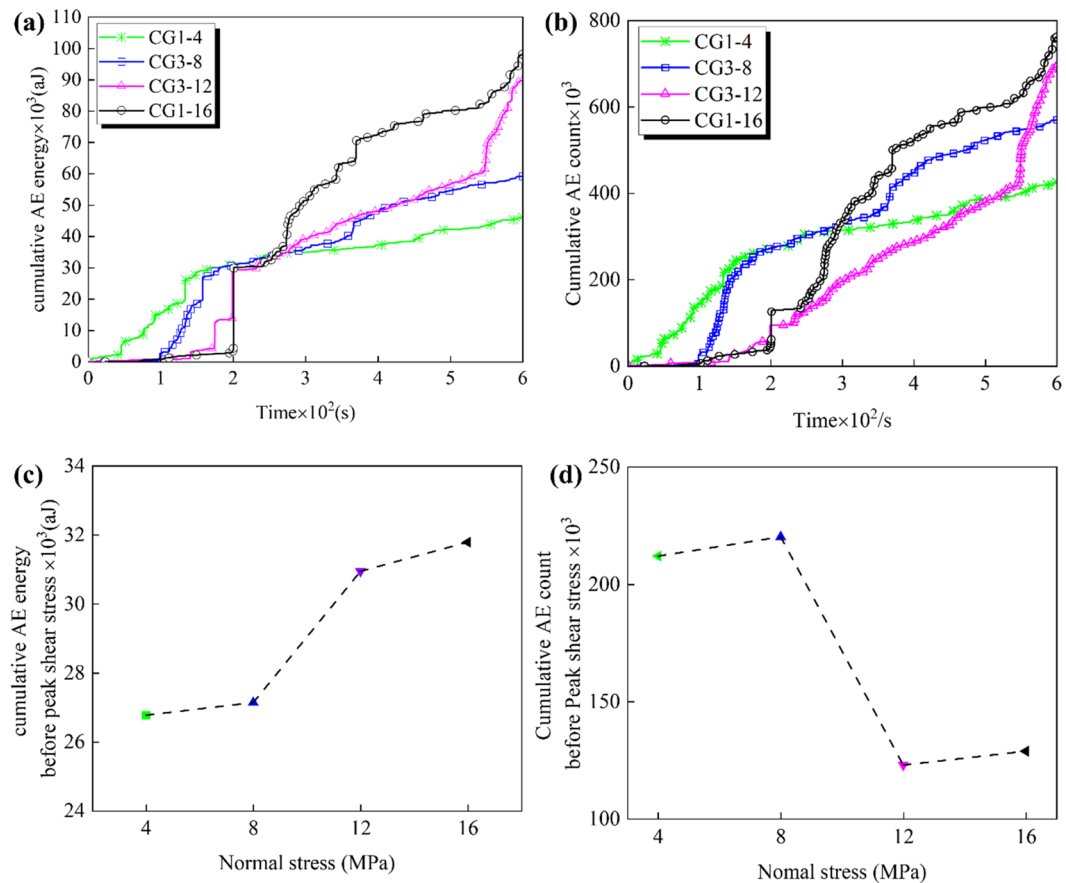


**Fig. 14.** The analysis encompasses the calculated cumulative acoustic emission (AE) energy and cumulative AE counts. Specifically, it includes: (a) a comparative assessment of cumulative AE energy curves, (b) a comparative evaluation of cumulative AE count curves, (c) the cumulative AE energy recorded prior to the peak shear stress, and (d) the cumulative AE peak counts observed before the peak shear stress.

$$\lg N = a - b \frac{A_{dB}}{20} \quad (3)$$

$$A_{dB} = 20 \lg A_{\mu V} \quad (4)$$

where  $A_{dB}$  indicates the maximum amplitude of acoustic emission (AE) events (dB),  $A_{\mu V}$  indicates the maximum amplitude of acoustic emission (AE) events ( $\mu V$ ),  $N$  represents the number of acoustic emission events with amplitudes greater than  $A_{dB}$ . The increase in  $b$ -value indicates the dominance of micro-cracks, while the decrease in  $b$ -value implies the dominance of macro-cracks. In addition, when  $b$ -value shows low frequency and small variation, it indicates that the micro-cracks extension is relatively stable. On the contrary, if  $b$ -value is showing high frequency and large fluctuation, it means that the micro-cracks are in the state of violent and frequent extension<sup>41–43</sup>.

In order to maintain stability and reliability, the  $b$ -value is calculated using an equal number of AE events (100 AE events) as the sampling window, and then a fixed number of AE events (50 AE events) are used as the step size to slide chronologically and repeat the  $b$ -value. The total number of acoustic emission events of CG1-4 specimen is 3429, the total number of acoustic emission events of CG3-8 specimen is 5005, the total number of acoustic emission events of CG3-12 specimen is 5323, and the total number of acoustic emission events of CG1-16 specimen is 7365. The stress-strain- $b$ -value relationship curves for the four specimens, derived from Eq. (2) to (4), are presented in Fig. 15. The characteristics of the evolution of AE  $b$ -values depicted in Fig. 15 indicate that the brittle failure at the rock-concrete interface is attributable to the initiation, progression, convergence, and penetration of internal micro-cracks, which in turn reflect the extent of energy release and damage.

In order to identify the phases where a spike in the rate of hits occurs, F-function based on inter-event time are used in this paper to analyze the fracture-related AE hit rate characteristics<sup>44]–[45</sup>. Firstly, a mean value  $\Delta t_i$  of the time interval between ( $N-1$ ) events is determined for each set of  $N$  consecutive hits ( $N \geq 10$ ) defined as follows:

$$\tau_i = \frac{\Delta t_i + \Delta t_{i+1} + \cdots + \Delta t_{i+N-2}}{N-1} = \frac{t_{N+i-1} - t_i}{N-1}, i = 1, 2, 3 \dots \quad (5)$$

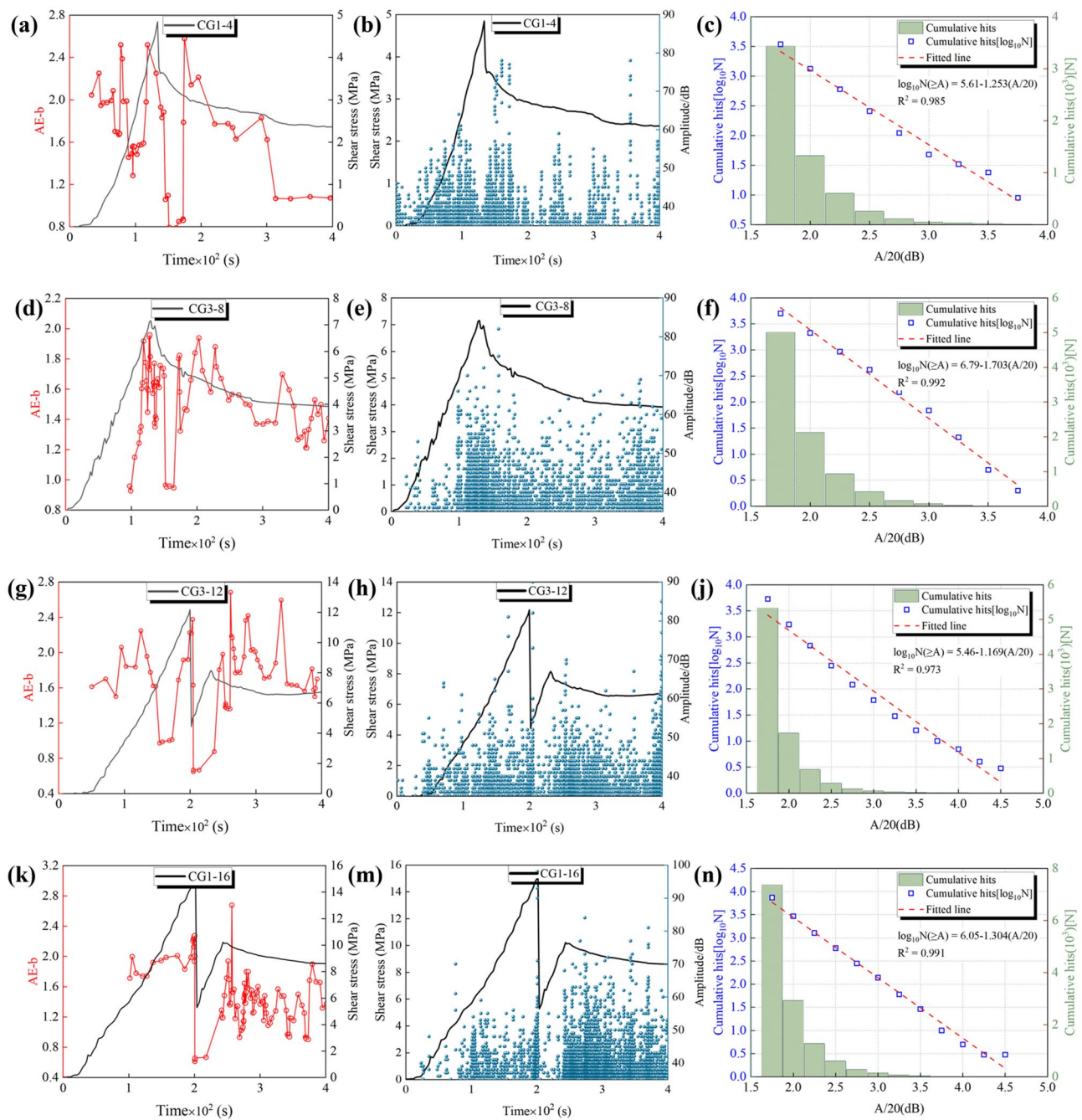


**Fig. 15.** Variation curves of calculated b-value.

where  $t_i$  and  $t_{N+i-1}$  indicate the moments of the  $i$  and  $N + i - 1$  AE events, respectively. The event interval time function  $F(\tau)$  within a given time window between  $t_i$  and  $t_{N+i-1}$  is defined as the reciprocal of  $\tau_i$ . The function  $F(\tau)$  of the time between events within a given time window between  $t_i$  and  $t_{N+i-1}$  is defined as the reciprocal of  $\tau_i$ :

$$F(\tau_i) = \tau_i^{-1}, i = 1, 2, 3 \dots \quad (6)$$

Each value of  $F(\tau)$  is then paired with the average value  $\bar{t}_i$  of the moment of occurrence of the corresponding  $N$  hits used to calculate the  $F$  function:

$$\bar{t}_i = \frac{t_i + t_{i+1} + \dots + t_{i+N-1}}{N}, i = 1, 2, 3 \dots \quad (7)$$

The specific pattern of evolution of F-function during the shearing process is shown in Fig. 16.

- (1) During the initial loading phase: b-value and F-function are hardly generated. This phenomenon indicates that the incidence of AE events and damage is relatively small.
- (2) Elastoplastic Deformation Stage: Initially, the b-value and F-function exhibited a slight increase, followed by a gradual upward trend characterized by increasing fluctuation frequency, whereas the curves at 12 MPa and 16 MPa were more sparser. Under conditions of low normal stress, the macro-fracture surface of the bonded interface results from the repeated transition between large-scale and small-scale micro-cracks, with the propagation and penetration of large-scale cracks occurring at a slow rate. In contrast, under higher normal stress conditions, the development of large-scale cracks at the rock-concrete interface is constrained by the normal stress, leading to a higher proportion of internal small-scale cracks compared to conditions of low normal stress. When the normal stress is inadequate to restrict shear deformation, the energy accumulated in the specimen during this stage is released rapidly over a short duration, resulting in the swift expansion of small-scale cracks at the rock-concrete interface and their penetration into large-scale cracks, thereby forming the primary fracture surface.
- (3) Instability Failure Stage: Upon reaching the stress peak, the b-value decreases sharply while the F-function increases sharply. It should be noted that the increase in AE event rate should precede the stress drop. This is because the increase in AE event rate is caused by microcrack nucleation, growth, and merging, while the stress drop is attributed to strain energy release due to macroscopic crack initiation and extension. The time interval between the increase in the AE event rate and the stress drop is difficult to distinguish due to the brittle nature of the specimen.

#### Variation of the AF-RA value in shear process

The quantitative differentiation of clusters of AE signals associated with tension or shear through the density distribution of RA-AF is challenging. The regions of RA and AF, as determined by acoustic emission experiments, exhibit significant overlap, which adversely affects the accuracy of crack identification during fracture processes. Consequently, this study employs a Gaussian mixture model (GMM) to cluster the AE feature parameters, facilitating a more precise quantitative separation of these clusters. Additionally, to address the limitations inherent in Gaussian mixture clustering regarding the quantitative differentiation of signals, a support vector machine (SVM) is utilized to compute the hyperplane delineating the clusters corresponding to each type of failure behavior. This approach enables the effective classification of tensile and shear signals<sup>46</sup>. As illustrated in Fig. 17, the frequency of shear failure signals in rock-concrete specimens surpasses that of tensile failure signals.

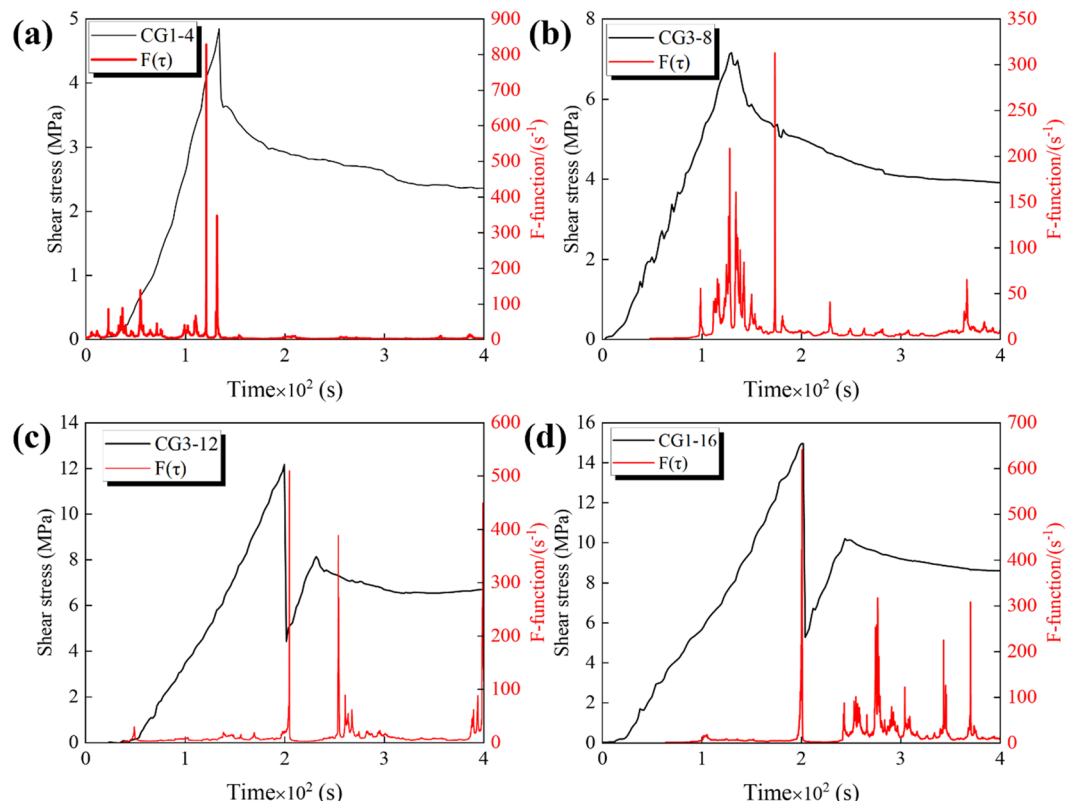


**Fig. 16.** The temporal variation of the F-function: (a) CG1-4, (b) CG3-8, (c) CG3-12, and (d) CG1-16.

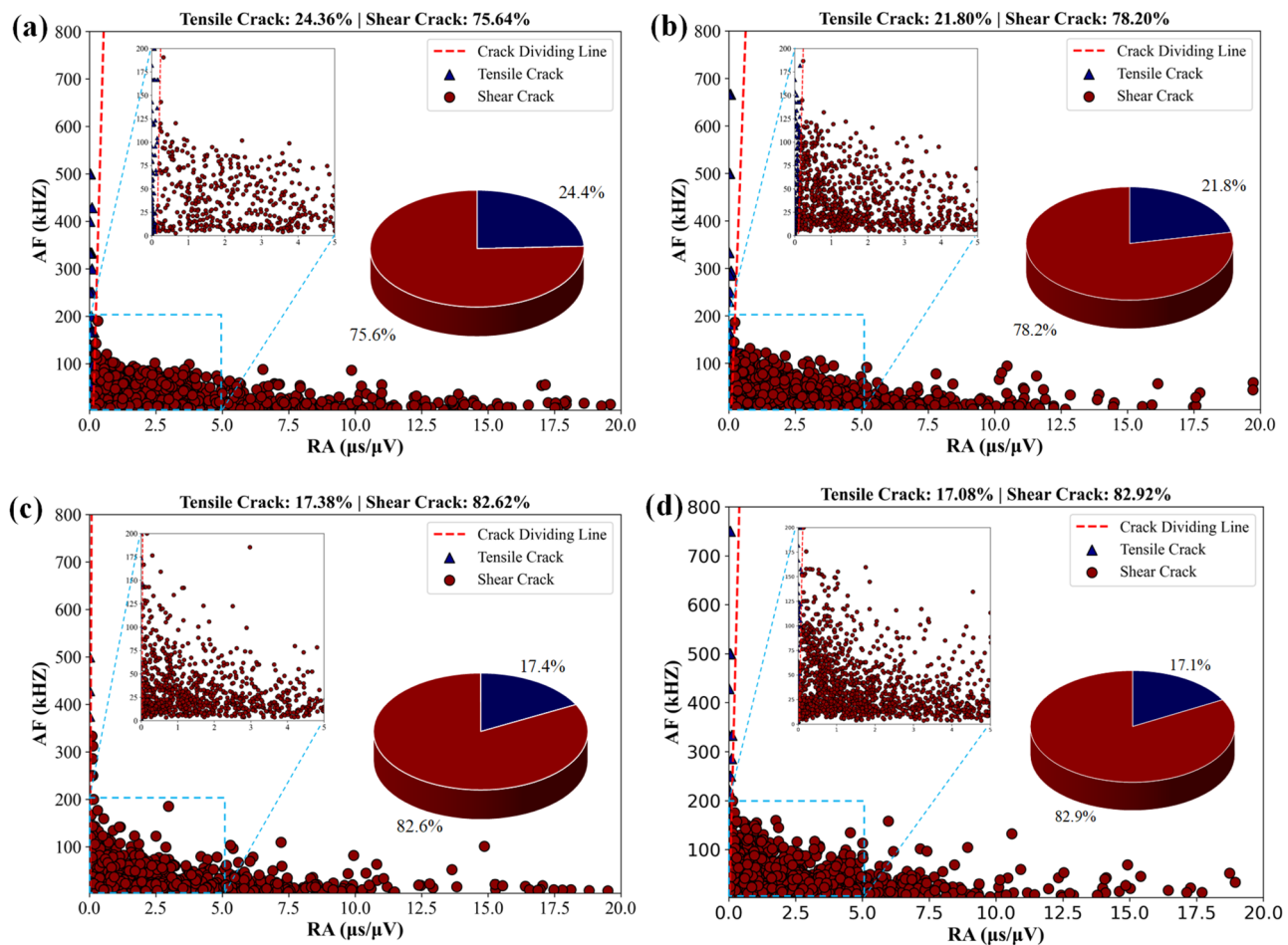


**Fig. 17.** The computed values of the RA-AF parameter are as follows: (a) CG1-4, (b) CG3-8, (c) CG3-12, and (d) CG1-16.

Furthermore, there is a notable trend indicating that the proportion of shear failure signals increases with rising normal stress.

## Discussion

A comparison with reference<sup>35</sup> reveals that the impact of normal stress on the degree of shear failure and the failure mode of the rock-concrete interface is less pronounced than that of surface roughness. In a non-bonding state, the application of shear displacement indicates that normal stress primarily enhances the frictional force at the interface, thereby increasing shear strength. In instances where the rock interface exhibits rough and undulating characteristics, normal stress facilitates a tighter interlocking between the rock and concrete, thereby augmenting both the anti-sliding force and the interlocking force at the bonding surface.

Analysis of the AE-b value demonstrates a marked difference in its evolution before and after the peak shear stress, which corresponds to the complete loss of adhesion between the rock and concrete. This observation indirectly elucidates the influence of the bonding force at the interface on the scale of cracking and the degree of fracture between the rock and concrete. Furthermore, the fluctuation range of the AE-b value at 16 MPa aligns with findings in reference<sup>35</sup>, indicating that the early warning capability of the AE-b value is more significantly influenced by normal stress than by the roughness of the rock interface, a consideration that warrants attention in practical applications.

In most practical scenarios, the normal load exerted on shotcrete linings typically does not exceed 0.2 to 0.5 MPa<sup>20</sup>. Consequently, the normal stress applied during shearing generally does not result in the crushing of the rock or concrete adjacent to the bonding surface. However, the four types of normal stresses examined in this study are substantial, leading to minimal variation in the shear fracture surface. Additionally, the high strength and certain roughness of the rock and concrete utilized in this research contribute to the cutting of rock or concrete protrusions under significant normal stress. Therefore, based on the test results, the author plans to conduct an orthogonal test on the natural roughness of rock for the shear failure of the rock-concrete interface under low normal stress, supplemented by numerical simulations for validation. Moreover, the shear rate is a critical factor influencing the shear failure behavior of the interface; the shear rate of 1 mm/min employed in

this study is relatively rapid for static load testing, necessitating further rock-concrete shear tests at varying shear rates.

## Conclusions

This study investigates the impact of varying normal stress on the shear failure characteristics of rock-concrete bonded interfaces, utilizing the RDS-200 direct shear apparatus. Furthermore, the study elucidates the mechanisms underlying crack propagation in rock-concrete systems through the application of the PCI-2 eight-channel acoustic emission device. The principal findings are summarized as follows:

- (1) An increase in normal stress results in enhanced peak shear strength, residual strength, and shear stiffness of the interface. Notably, the post-peak softening behavior transitions from a gradual reduction in stress, indicative of ductile failure, to a rebound mode characterized by a 'double peak stress' phenomenon, which is representative of brittle failure, when normal stresses exceed 12 MPa. In contrast, lower normal stresses ( $\leq 8$  MPa) induce shear expansion deformation, whereas higher normal stresses ( $\geq 12$  MPa) lead to shear contraction deformation.
- (2) The influence of normal stresses on the modes of interface damage is relatively minimal, as all observed modes are classified as mixed ARC damage modes. However, the extent of interface damage is observed to increase with rising normal stresses, while the residual concrete coverage on the rock surface remains stable at approximately 30%.
- (3) High acoustic emission (AE) energy signals and counts are recorded at the peak shear stress. The cumulative AE energy prior to failure exhibits a slight increase with normal stress, whereas the cumulative AE counts show a decrease, suggesting that microcracking activity is inhibited under elevated normal stresses prior to the failure of the specimens.
- (4) The evolution of cracks is effectively represented by the b-value and F-function: a pronounced decline at peak stress correlates with brittle damage, and both the amplitude and frequency of pre-peak fluctuations diminish as normal stress increases, indicating a reduction in crack propagation at elevated normal stresses. Furthermore, the proportion of shear damage signals in the specimens, as determined by the combined Gaussian Mixture Model (GMM) and Support Vector Machine (SVM), exceeds 75% and increases with the escalation of normal stress.

## Data availability

The data sets used in the current study are available from the corresponding author on reasonable request.

Received: 27 June 2024; Accepted: 31 July 2025

Published online: 08 August 2025

## References

1. Wang, T. Characterizing crack patterns on tunnel linings associated with shear deformation induced by instability of neighboring slopes. *Eng. Geol.* **115** (1–2), 80–95. <https://doi.org/10.1016/j.enggeo.2010.06.010> (2010).
2. Chen, Y. & Li, C. Performance of fully encapsulated rebar bolts and D-Bolts under combined pull-and-shear loading. *Tunn. Undergr. Sp. Tech.* **45**, 99–106. <https://doi.org/10.1016/j.tust.2014.09.008> (2015).
3. Yin, Q., Liu, R., Jing, H., Su, H. & He, L. Experimental study of nonlinear flow behaviors through fractured rock samples after High-Temperature exposure. *Rock. Mech. Rock. Eng.* **52**, 2963–2983. <https://doi.org/10.1007/s00603-019-1741-0> (2019).
4. Song, Z., Cheng, Y., Zhang, Z. & Yang, T. Tunnelling performance prediction of cantilever boring machine in sedimentary hard-rock tunnel using deep belief network. *J. Mt. Sci.* **20**, 2029–2040. <https://doi.org/10.1007/s11629-023-7931-y> (2023).
5. Cheng, Y. et al. Micro-cracking morphology and dynamic fracturing mechanism of natural brittle sandstone containing layer structure under compression. *Constr. Build. Mater.* **425** <https://doi.org/10.1016/j.conbuildmat.2024.136051> (2024).
6. Cheng, Y., Song, Z. & Xu, Z. Failure mechanism and infrared radiation characteristic of hard siltstone induced by stratification effect. *J. Mt. Sci.* **21**, 1058–1074. <https://doi.org/10.1007/s11629-023-8444-4> (2024).
7. Zhao, W., Chen, W. & Zhao, K. Laboratory test on foamed concrete-rock joints in direct shear. *Constr. Build. Mater.* **173** (10), 69–80. <https://doi.org/10.1016/j.conbuildmat.2018.04.006> (2018).
8. Hong, C. & Jeon, S. Influence of shear load on the characteristics of acoustic emission of rock-concrete interface. *Key Eng. Mater.* 270–273. <https://doi.org/10.4028/www.scientific.net/kem.270-273.1598> (2004).
9. Moradian, Z., Ballivy, G., Rivard, P., Gravel, C. & Rousseau, B. Evaluating damage during shear tests of rock joints using acoustic emissions. *Int. J. Rock. Mech. Min. Sci.* **47** (4), 590–598. <https://doi.org/10.1016/j.ijrmms.2010.01.004> (2010).
10. Moradian, Z., Ballivy, G. & Rivard, P. Application of acoustic emission for monitoring shear behavior of bonded concrete-rock joints under direct shear test. *Can. J. Civil Eng.* **39** (8), 887–896. <https://doi.org/10.1139/L2012-073> (2012).
11. Seidel, J. & Haberfield, C. A theoretical model for rock joints subjected to constant normal stiffness direct shear. *Int. J. Rock. Mech. Min. Sci.* **39** (5), 539–553. [https://doi.org/10.1016/S1365-1609\(02\)00056-4](https://doi.org/10.1016/S1365-1609(02)00056-4) (2002).
12. Zhu, J., Bao, W. & Peng, Q. Influence of substrate properties and interfacial roughness on static and dynamic tensile behaviour of rock-shotcrete interface from macro and micro views. *Int. J. Rock. Mech. Min. Sci.* **132**, 104350. <https://doi.org/10.1016/j.ijrmms.2020.104350> (2020).
13. Liu, S., Zhang, Q. & Ma, B. Study on surface roughness effect on shear behavior of concrete-soil interface. *Eng. Fail. Anal.* **145**, 107050. <https://doi.org/10.1016/j.engfailanal.2023.107050> (2023).
14. Hu, Z. et al. Study on shear failure characteristics of fiber-reinforced shotcrete-granite interface based on surface scanning. *Case Stud. Constr. Mater.* **21**, e03486. <https://doi.org/10.1016/j.cscm.2024.e03486> (2024).
15. Park, J. & Song, J. Numerical method for the determination of contact areas of a rock joint under normal and shear loads. *Int. J. Rock. Mech. Min. Sci.* **58**, 8–22. <https://doi.org/10.1016/j.ijrmms.2012.10.001> (2013).
16. Bahaaeddini, M., Hagan, P., Mitra, R. & Hebblewhite, B. Scale effect on the shear behaviour of rock joints based on a numerical study. *Eng. Geol.* **181**, 212–223. <https://doi.org/10.1016/j.enggeo.2014.07.018> (2014).
17. Bahaaeddini, M., Hagan, P., Mitra, R. & Khosravi, M. Experimental and numerical study of asperity degradation in the direct shear test. *Eng. Geol.* **204**, 41–52. <https://doi.org/10.1016/j.enggeo.2016.01.018> (2016).
18. Zhao, Z., Jing, L. & Neretnieks, I. Particle mechanics model for the effects of shear on solute retardation coefficient in rock fractures. *Int. J. Rock. Mech. Min. Sci.* **52**, 92–102. <https://doi.org/10.1016/j.enggeo.2016.01.018> (2012).

19. Gu, X., Seidel, J. & Haberfield, C. Direct shear test of sandstone concrete joints. *Int. J. Geomech.* **3** (1–2), 21–33 (2003). 10.1061/(ASCE)1532-3641(2003)3:1(21).
20. Saiang, D., Malmgren, L. & Norflund, E. Laboratory test on shotcrete-rock joints in direct shear, tension and compression. *Rock. Mech. Rock. Eng.* **38**, 275–297. <https://doi.org/10.1007/s00603-005-0055-6> (2005).
21. Tian, H., Chen, W., Yang, D. & Yang, J. Experimental and numerical analysis of the shear behavior of cemented concrete–rock joints. *Rock. Mech. Rock. Eng.* **48**, 213–222. <https://doi.org/10.1007/s00603-014-0560-6> (2015).
22. Bost, M., Mouzannar, H. & Rojat, F. Metric scale study of the bonded Concrete–Rock interface shear behaviour. *KSCE J. Civ. Eng.* **24**, 390–403. <https://doi.org/10.1007/s12205-019-0824-5> (2020).
23. Mouzannar, H., Bost, M., Leroux, M. & Virely, D. Experimental study of the shear strength of bonded concrete–rock interfaces: surface morphology and scale effect. *Rock. Mech. Rock. Eng.* **50** (10), 2601–2625. <https://doi.org/10.1007/s00603-019-01951-0> (2017).
24. Johansson, F. Influence of scale and matedness on the peak shear strength of fresh, unweathered rock joints. *Int. J. Rock. Mech. Min. Sci.* **82**, 36–47. <https://doi.org/10.1016/j.ijrmms.2015.11.010> (2016).
25. Sun, Y., Sumelka, W. & Gao, Y. Phenomenological fractional stress–dilatancy model for granular soil and soil–structure interface under monotonic and Cyclic loads. *Acta Geotech.* **16**, 3115–3132. <https://doi.org/10.1007/s11440-021-01190-0> (2021).
26. Alonso, E., Josa, A. & Ledesma, A. Negative skin friction on piles: A simplified analysis and prediction procedure. *Geotech* **34** (3), 341–357. [https://doi.org/10.1016/0148-9062\(85\)92825-6](https://doi.org/10.1016/0148-9062(85)92825-6) (1984).
27. Liu, R., Zhu, X. & Zhang, Y. Simultaneous unloading of shear and normal stresses induces activation of naturally rough-walled sandstone fractures. *Int. J. Rock. Mech. Min. Sci.* **170**, 105488. <https://doi.org/10.1016/j.ijrmms.2023.105488> (2023).
28. Wu, W. & Zhao, J. A dynamic-induced direct-shear model for dynamic triggering of frictional slip on simulated granular particles. *Exp. Mech.* **54** (4), 605–613. <https://doi.org/10.1007/s11340-013-9823-5> (2014).
29. Cai, M. et al. Back-analysis of rock mass strength parameters using AE monitoring data. *Int. J. Rock. Mech. Min. Sci.* **44** (4), 538–549. <https://doi.org/10.1016/j.ijrmms.2006.09.012> (2007).
30. Ji, S. & Di, S. Discrete element modeling of acoustic emission in rock fracture. *TAML* **3** (2). <https://doi.org/10.1063/2.1302109> (2013).
31. Rao, M. & Lakshmi, K. Analysis of B-Value and improved b-Value of acoustic emissions accompanying rock fracture. *Curr. Curr. Sci.* **89** (9), 1577–1582 (2005). <http://www.jstor.org/stable/24110936>
32. Changwoo, H. & Seokwon, J. Influence of shear load on the characteristics of acoustic emission of rock-concrete interface. *Key Eng. Mater.* **270**–273. <https://doi.org/10.4028/www.scientific.net/kem.270-273.1598> (2004).
33. Gan, Y., Wu, S., Ren, Y. & Zhang, G. Evaluation indexes of granite splitting failure based on RA and AF of AE parameters. *Rock. Soil. Mech.* **41**, 2324–2332. <https://doi.org/10.16285/j.rsm.2019.1460> (2020).
34. Cheng, Y. et al. Micro-cracking morphology and dynamic fracturing mechanism of natural brittle sandstone containing layer structure under compression. *Constr. Build. Mater.* **425**, 136051. <https://doi.org/10.1016/j.conbuildmat.2024.136051> (2024).
35. Chen, Y. et al. Effects of roughness on shear properties and acoustic emission characteristics of bonded Rock-Concrete interfaces. *Constr. Build. Mater.* **398**, 132405. <https://doi.org/10.1016/j.conbuildmat.2023.132405> (2023).
36. Liu, X., Liu, Z., Li, X., Gong, F. & Du, K. Experimental study on the effect of strain rate on rock acoustic emission characteristics. *Int. J. Rock. Mech. Min. Sci.* **133**, 104420. <https://doi.org/10.1016/j.ijrmms.2020.104420> (2020).
37. Zhou, H. et al. Investigation of the acoustic emission characteristics of artificial saw-tooth joints under shearing condition. *Acta Geotech.* **11** (4), 925–939. <https://doi.org/10.1007/s11440-014-0359-3> (2016).
38. Gutenberg, B. & Richter, C. Frequency of earthquakes in California. *Nature* **156**–371. <https://doi.org/10.1038/156371a0> (1945).
39. Lei, X. Evolution of b-value and fractal dimension of acoustic emission events during shear rupture of an immature fault in granite. *Appl. Sci.* **9** (12). <https://doi.org/10.3390/app9122498> (2019).
40. Chen, Y. & Zhao, Z. Correlation between shear induced asperity degradation and acoustic emission energy in single granite fracture. *Eng. Frac. Mech.* **235**, 107184. <https://doi.org/10.1016/j.engfracmech.2020.107184> (2020).
41. Vidya, R., Raghu, B. & Shanta, S. An experimental study on cracking evolution in concrete and cement mortar by the b-value analysis of acoustic emission technique. *Cem. Concr. Res.* **42** (8), 1094–1104. <https://doi.org/10.1016/j.cemconres.2012.05.003> (2012).
42. Triantis, D. & Kourkoulis, S. Fracture precursor phenomena in marble specimens under uniaxial compression by means of acoustic emission data. *Frac. Struct. Integr.* **13** (50), 537–547. <https://doi.org/10.3221/IGF-ESIS.50.45> (2019).
43. Vidya, R. A parallel between earthquake sequences and acoustic emissions released during fracture process in reinforced concrete structures under flexural loading. *Constr. Build. Mater.* **114**, 772–793. <https://doi.org/10.1016/j.conbuildmat.2016.03.082> (2016).
44. Triantis, D. & Kourkoulis, S. An Alternative Approach for Representing the Data Provided by the Acoustic Emission Technique, *Rock. Mech. Rock. Eng.* **51**, 2433–2438. <https://doi.org/10.1007/s00603-018-1494-1>. (2018).
45. Triantis, D., Pasiou, E. & Stavrakas, I. Hidden affinities between electric and acoustic activities in brittle materials at Near-Fracture load levels. *Rock. Mech. Rock. Eng.* **55**, 1325–1342. <https://doi.org/10.1007/s00603-021-02711-9> (2022).
46. Jiao, Y., Chen, Y., Yang, H. & Wang, C. Experimental characterization on fracture behavior of UHPC under small-scale sample tensile testing: acoustic emission monitoring and digital image correlation. *Theor. Appl. Fract. Mec.* **130**, 104342. <https://doi.org/10.1016/j.tafmec.2024.104342> (2024).

## Acknowledgements

Financial supports from the Henan Science and Technology Research Project (242102321163), Key Scientific Research Project of Higher Education Institutions in Henan Province (24A440004), the National Natural Science Foundation of China (51904092, 52104089, 52274078), the Fundamental Research Funds for the Universities of Henan Province (NSFRF230403), Young backbone teachers funding program of Henan Polytechnic University (2022XQG-01) and the research fund of Henan Key Laboratory for Green and Efficient Mining & Comprehensive Utilization of Mineral Resources (KCF2202) are gratefully acknowledged.

## Author contributions

Y. C.: Conceptualization, Investigation, Writing—original draft, Project administration, Funding acquisition. J. F.: Methodology, Software, Validation. J. W.: Writing—review and editing. S. H.: Writing—review and editing. Z. H.: Software, Validation, Data curation.

## Declarations

### Competing interests

The authors declare no competing interests.

### Additional information

Correspondence and requests for materials should be addressed to Y.C.

Reprints and permissions information is available at [www.nature.com/reprints](http://www.nature.com/reprints).

**Publisher's note** Springer Nature remains neutral with regard to jurisdictional claims in published maps and institutional affiliations.

**Open Access** This article is licensed under a Creative Commons Attribution-NonCommercial-NoDerivatives 4.0 International License, which permits any non-commercial use, sharing, distribution and reproduction in any medium or format, as long as you give appropriate credit to the original author(s) and the source, provide a link to the Creative Commons licence, and indicate if you modified the licensed material. You do not have permission under this licence to share adapted material derived from this article or parts of it. The images or other third party material in this article are included in the article's Creative Commons licence, unless indicated otherwise in a credit line to the material. If material is not included in the article's Creative Commons licence and your intended use is not permitted by statutory regulation or exceeds the permitted use, you will need to obtain permission directly from the copyright holder. To view a copy of this licence, visit <http://creativecommons.org/licenses/by-nc-nd/4.0/>.

© The Author(s) 2025